ADVANCED FUNCTIONAL MATERIALS

Supporting Information

for *Adv. Funct. Mater.*, DOI 10.1002/adfm.202314761

Promising VO_2(B)/rGO Heterojunction Cathode for Building High-Capacity and Long-Lifespan Ca-Ion Batteries

Yu Wang, Junjun Wang, Wenwei Zhang, Feiyang Chao, Jinghao Li, Qinghong Kong, Fan Qiao, Lei Zhang, Meng Huang* and Qinyou An**

Supporting Information

Promising VO_2(B)/rGO heterojunction cathode for building high-capacity and long-lifespan Ca-ion batteries

Yu Wang, Junjun Wang, Wenwei Zhang, Feiyang Chao, Jinghao Li, Qinghong Kong, Fan Qiao, Lei Zhang, Meng Huang,* Qinyou An**

Experimental Section

Synthesis of VO_2(B)

VO_2(B) nanobelt was synthesized by a one-step hydrothermal method. Firstly, 0.6 g V_2O_5 and 20 ml ethylene glycol were added to 60 ml ultra-pure water and then the above solution was stirred at room temperature for 30 min. Afterwards, the obtained solution was transferred into a 100 ml Teflon-lined autoclave. The sealed autoclave was put into an oven at 180 °C for 10 h. Finally, the dark gray products were centrifuged and washed with deionized water and absolute ethanol several times. The obtained product was dried in a vacuum drying oven at 60 °C for one night.

Synthesis of VO_2(B)/rGO

The VO_2(B)/rGO composite was synthesized by ultrasonication combined with the freeze-drying method. 0.2 g of as-prepared VO_2(B) powder and 3 ml GO suspension were dispersed into 15 ml of deionized water and stirred for 2 h. GO was purchased from Jiangsu XFNANO Materials Tech Co., Ltd. Subsequently, the homogeneous dispersion liquid was subjected to ultrasonic synthesis for 2 h. Finally, the obtained solution was freeze-dried for 3 days until all of the water was sublimated, and the remaining powder obtained was the VO_2(B)/rGO composite.

Synthesis of Polyaniline (PANI)

Stir 0.4 ml of aniline monomer in dichloromethane (40 ml) for 30 min to form Solution A. Add 0.5 g of ammonium persulfate to 40 ml of 0.5 M HCl and stir for 30 min to form Solution B. Mix Solutions A and B together. Keep the reaction system at 5 °C for 24 h. Wash with deionized water and ethanol, and finally vacuum dry at 60 °C for 8 h.

Characterization Methods

In-situ XRD measurement was performed using a Bruker AXS D8 Advance powder X-ray diffractometer with an area detector using a Cu Kα X-ray source. *Ex-situ* and powder XRD measurement was performed using a Bruker AXS D2 Advance powder X-ray diffractometer with a detector using Cu Kα X-ray source. Scanning electron microscope (SEM) images were acquired by using a JEOL-7100F microscope. A Titan G2 60-300 instrument was used for transmission electron microscopy (TEM), high-resolution TEM, high-angle annular dark field (HAADF) images and energy dispersive X-ray spectroscopy (EDX) maps tests. Kratos AXIS SUPRA instrument was used for XPS measurement. Ar^+ etching can be performed using the ion gun provided with the equipment. Thermogravimetric analysis (TGA) was carried out on a NETZSCH-STA449F5 thermo-analyzer with a heating rate of 10 ˚C min^{-1} in an air atmosphere. Fourier Transform Infrared Spectroscopy (FTIR) transmittance spectra and *in-situ* FTIR were carried out by a Nicolet 6700 (Thermo Fisher Scientific Co., USA) IR spectrometer. CHNS(O) was employed on Elementar UNICUBE. The BET surface area was calculated from nitrogen adsorption isotherms collected at 77 K using a Tristar-3020 instrument. *Ex-situ* and powder Raman characterizations were measured with a green laser (532 nm) using the LABRAM HR Evolution Raman spectrometer. The time-of-flight-secondary ion mass spectrometry (TOF-SIMS) measurements were performed using a PHI nano TOF 3 to analyze electrode film depth profiles. The measurements were conducted with a bismuth (Bi) liquid metal primary ion gun (LMIG).

Electrochemical Measurements

The positive electrode consists of VO_2(B)/rGO (70 wt%), acetylene black (AB, 20 wt%), and polytetrafluoroethylene (PTFE, 10 wt%). Grind them into a uniform mixture and press them into thin sheets. The mass loading of the cathode keeps 2-2.5 mg cm^{-2}. The as-prepared electrodes were dried under 60 ℃ for one night. Finally, the Ca^{2+} storage performances of VO_2(B)/rGO were tested by CR 2016 coin cell assembled in an argon-filled glove box (<1 ppm of water and oxygen) with the prepared positive electrode, GF/A as separator, 0.3 M $Ca(TFSI)_2$ in tetraethylene glycol dimethyl ether (G4) as the electrolyte and ACC (1500-2500 m^2 g^{-1} GUN EI Chemical Industry Co. Ltd.) as both reference and counter electrode. The loading of active materials on the cathode is about 1.0 mg cm^{-2} and the loading of ACC (12 mm diameter) is about 16.0 mg cm^{-2}. Electrochemical performance measurement with $Ca(TFSI)_2$ based electrolyte was conducted at 50 ℃ and room temperature. A multichannel battery testing system (LAND CT 2001A) was used. Cyclic voltammetry (CV) tests were performed with an Auto-lab

PGSTAT 302N electrochemical workstation. Electrochemical impedance spectroscopy (EIS) was tested from 0.01 Hz to 100 KHz with an amplitude of 10 mV via Auto-lab PGSTAT 302N. *In-situ* XRD, e*x-situ* XRD, *ex-situ* XPS, and *ex-situ* Raman tests were carried out at room temperature.

Calculation Method

A series of calculations based on density functional theory were completed using the Vienna Ab initio Simulation Package (VASP) [1]. The embedding of Ca^{2+} into the internal hollow space of VO_2(B) bulks was simulated. For all calculations, Perdew-Burke-Ernzerhof exchange-correlation functional [2] was used with spin polarization. The plan-wave cutoff energy of 520 eV for the projector augmented wave (PAW) method [3] and Gamma point centered k-mesh in the Brillouin zone with separation of $0.04\times2\pi$ $Å^{-1}$ were set. The Grimme-D3 method [4] was applied to correct the dispersion force and the Climbing Image Nudged Elastic Band (CI-NEB) method [5] was used to simulate the migration of different particles. The energy difference should be lower than 10^{-5} eV/atom to reach electronic self-consistent field convergence, and the force should be lower than 0.02 eV/Å to reach the convergence for the ionic step in geometric optimizations. The cell lattices of VO_2(B) bulks were relaxed when embedded with particles. The VO_2(B) bulks contain 64 O and 32 V atoms.

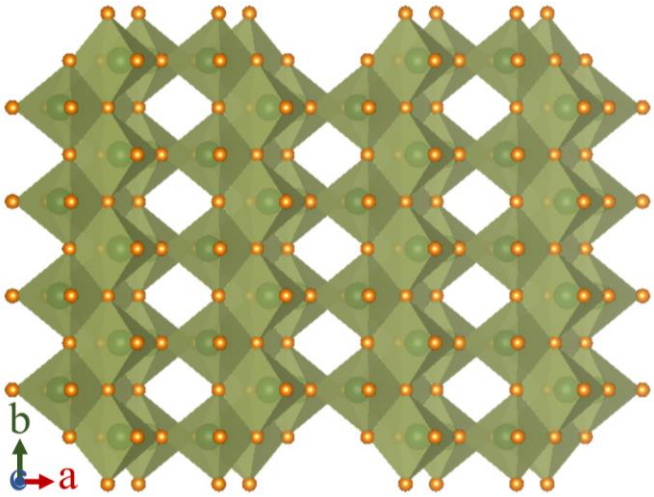

Figure S1. Crystal structure of VO_2(B) phase.

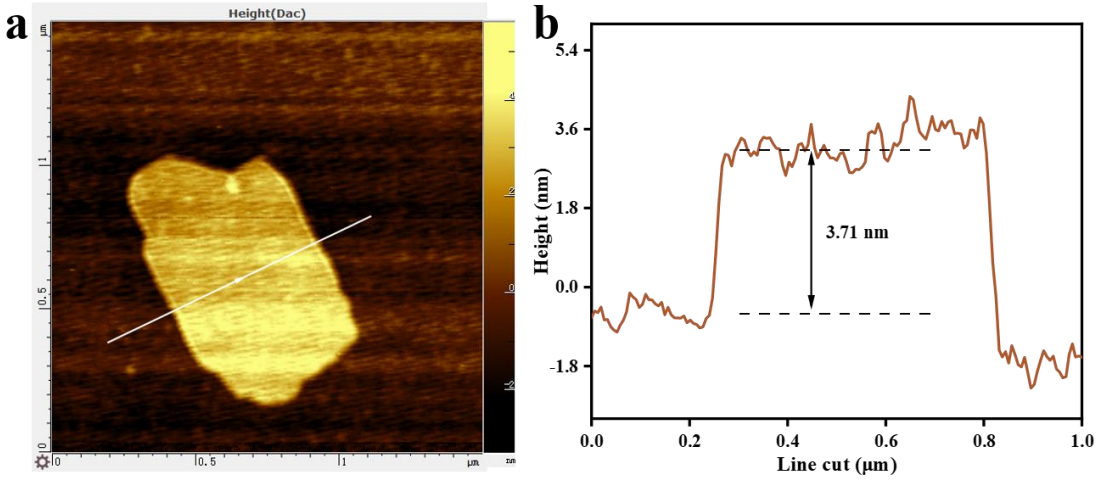

Figure S2. a) AFM image of GO nanosheets; b) Corresponding line section profile.

Atomic Force Microscopy (AFM) analysis shows a height of 3.71 nm, indicative of 3-5 GO layers.

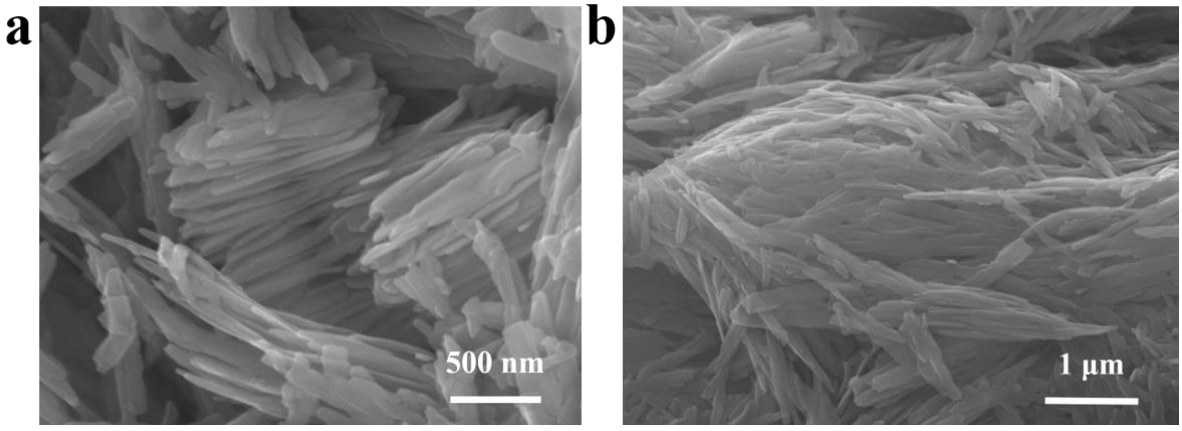

Figure S3. SEM images of a) VO_2(B) and b) VO_2(B)/rGO.

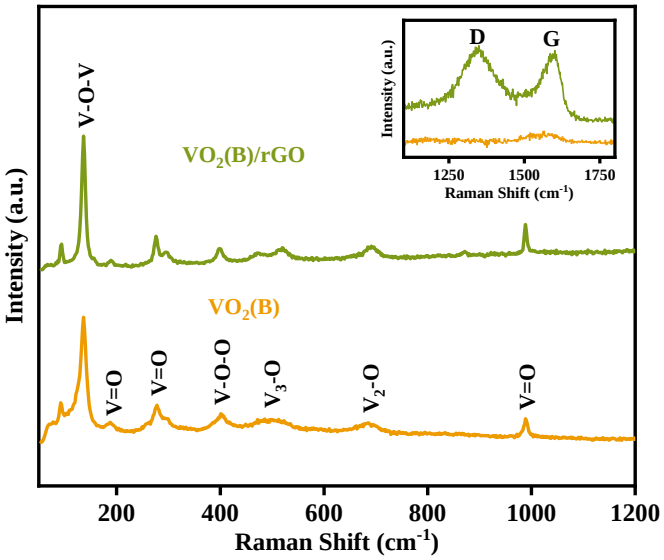

Figure S4. Raman spectra of VO_2(B) and VO_2(B)/rGO.

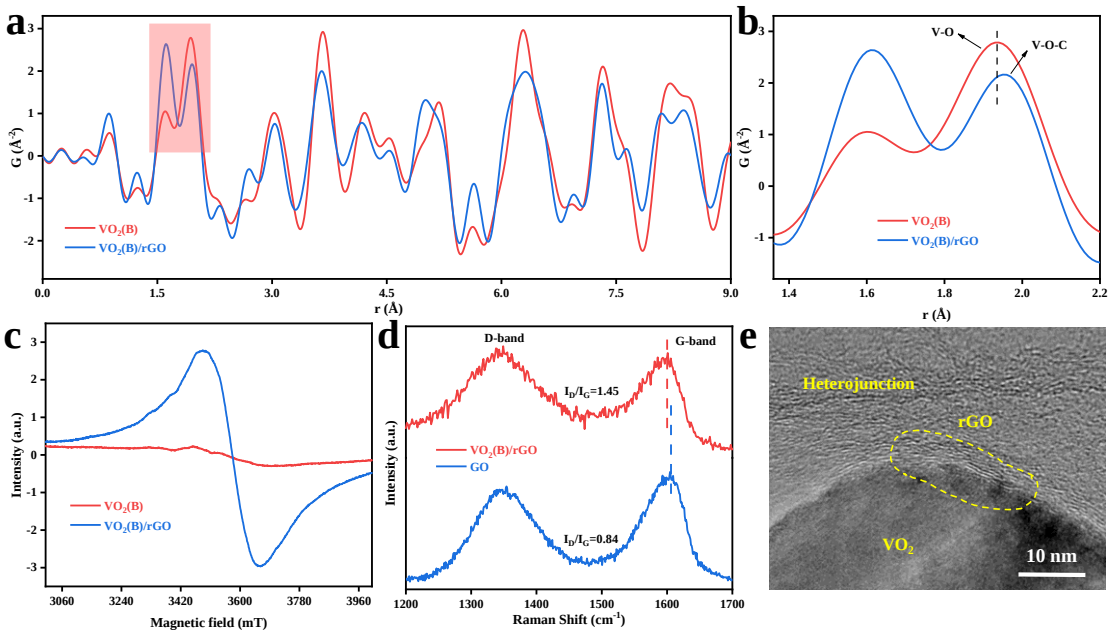

Figure S5. a) Pair distribution function of VO_2(B) and VO_2(B)/rGO; b) An enlarged view of the selected region from Figure S5a; c) EPR spectra of VO_2(B) and VO_2(B)/rGO; d) Raman spectra of GO and VO_2(B)/rGO. e) HRTEM image of VO_2(B)/rGO.

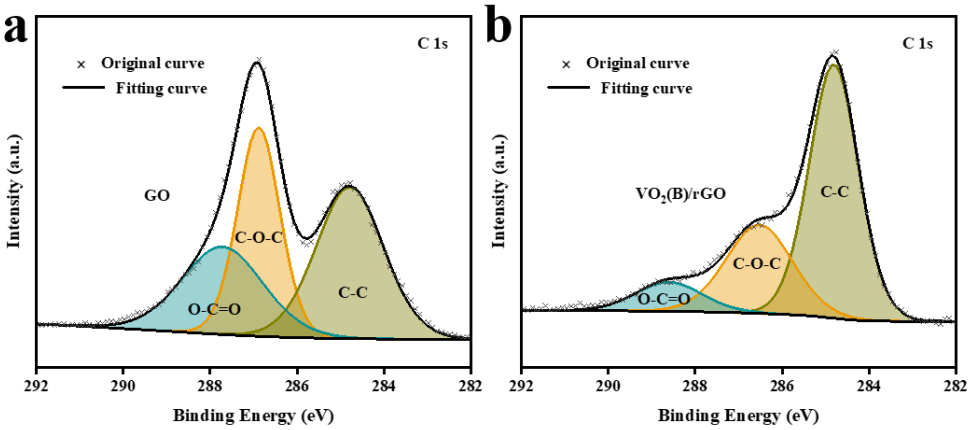

Figure S6. XPS spectrum of C 1s of a) GO and b) VO_2(B)/rGO powder.

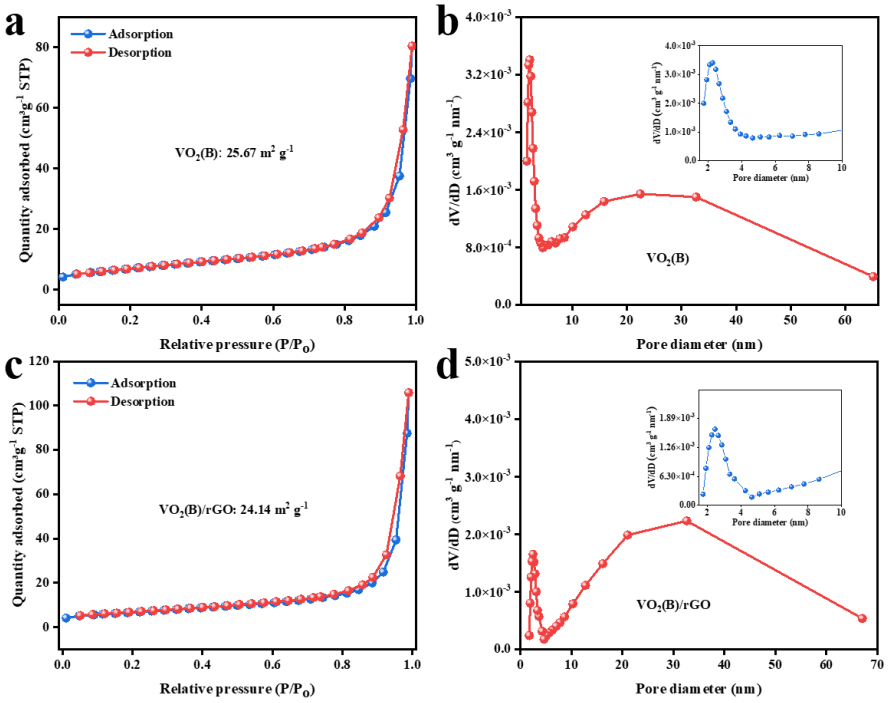

Figure S7. The nitrogen adsorption–desorption isotherm curve of a) VO_2(B) and c) VO_2(B)/rGO powder; The corresponding pore size distribution of b) VO_2(B) and d) VO_2(B)/rGO.

Table S1. The quantitative elemental ratios of VO_2(B)/rGO.

	N（%）	C（%）	H（%）	S（%）
First Test	0.086	2.598	0.759	0.103
Second Test	0.102	2.591	0.747	0.105

In order to minimize data inaccuracies, the sample is subjected to duplicate testing.

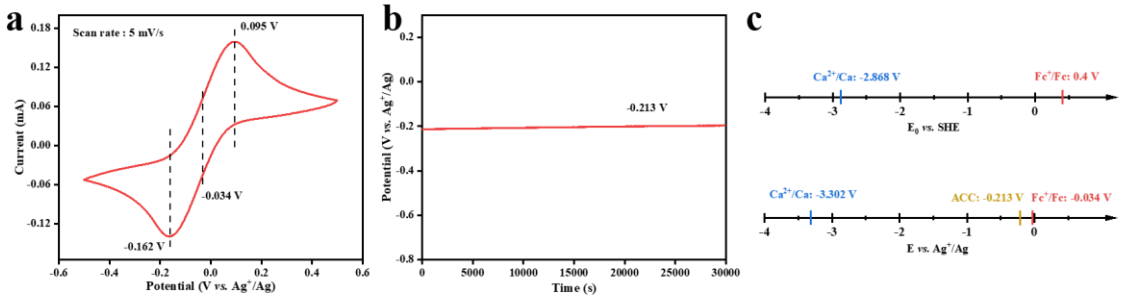

Figure S8. a) CV of Ferrocene in 0.3 M $Ca(TFSI)_2$/G4 electrolyte in a three-electrode system. b) Open circuit potential of the ACC *vs.* Ag^+/Ag reference electrode in 0.3 M $Ca(TFSI)_2$/G4 electrolyte. c) Comparison of electrochemical potentials.

Figure S8a indicates the redox potential of Fc/Fc^+ *vs.* Ag^+/Ag is approximately at –0.034 V. Figure S8b shows that the potential of ACC *vs.* Ag^+/Ag is -0.213 V. Figure S8c indicates that the potential difference between Ca^{2+}/Ca and Fc^+/Fc is 3.268 V, from which it can be inferred that the potential of Ag^+/Ag *vs.* Ca^{2+}/Ca is 3.302 V. Consequently, the potential of ACC *vs.* Ca^{2+}/Ca is determined to be 3.089 V.

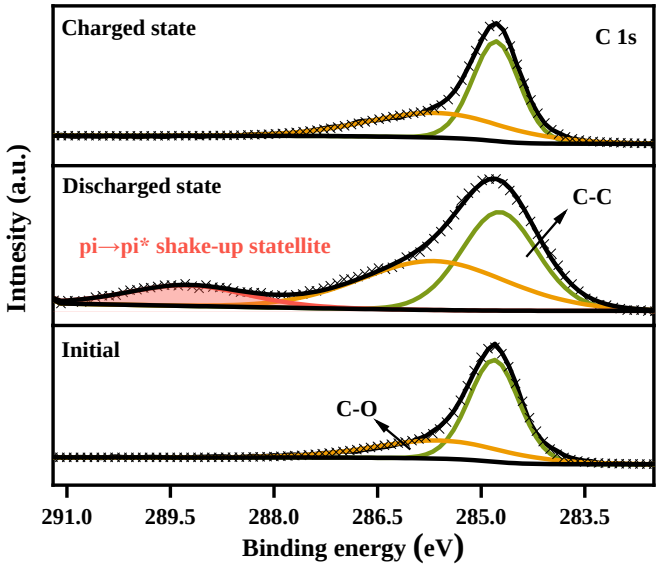

Figure S9. *Ex-situ* XPS spectra of C 1s for VO_2(B)/rGO at different states.

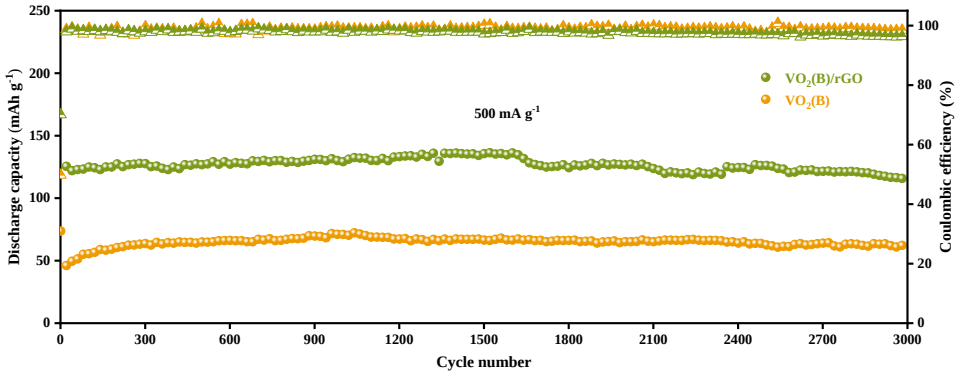

Figure S10. Cycling performances of VO_2(B) and VO_2(B)/rGO at 500 mA g^{-1} and room temperature.

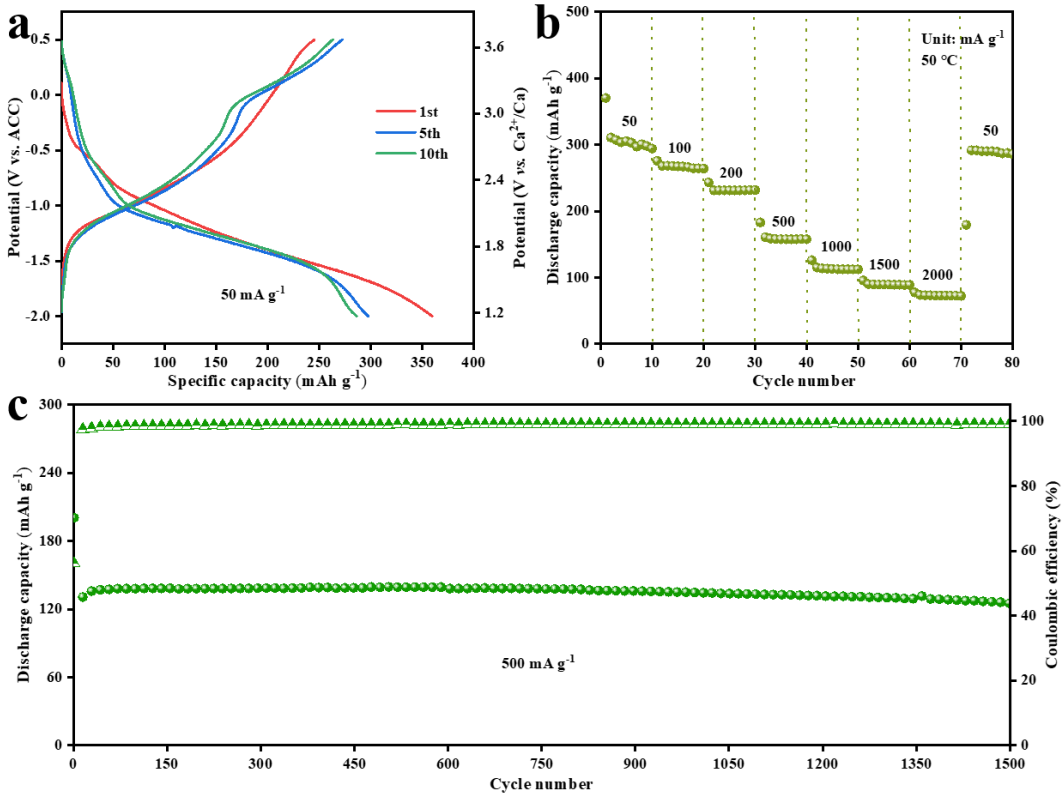

Figure S11. The electrochemical performance of VO_2(B)/rGO at 50 °C. a) Galvanostatic charge/discharge profiles at 50 mA g^{-1}; b) Rate performance at various current densities; c) Cycling performance at 500 mA g^{-1}.

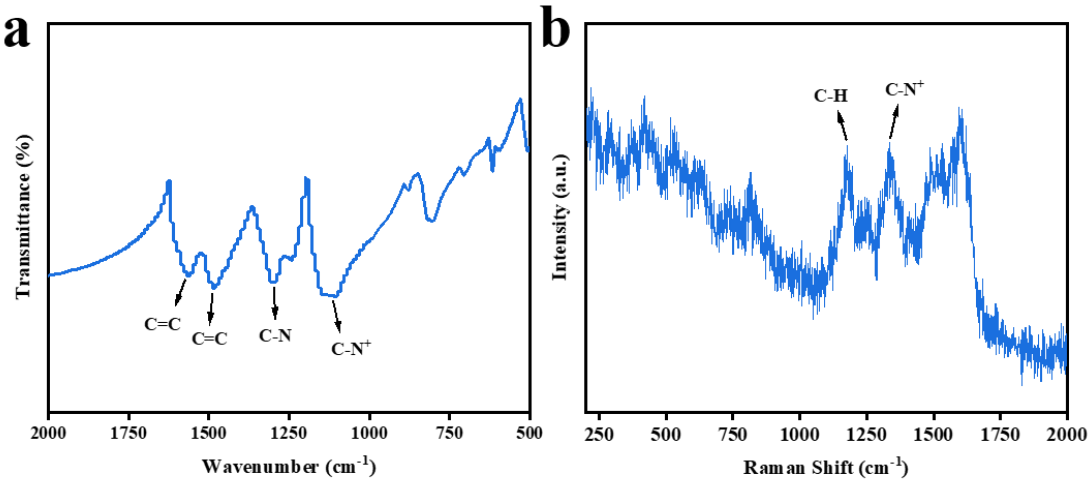

Figure S12. Structure and characterization of PANI. a) FT-IR spectrum; b) Raman spectrum.

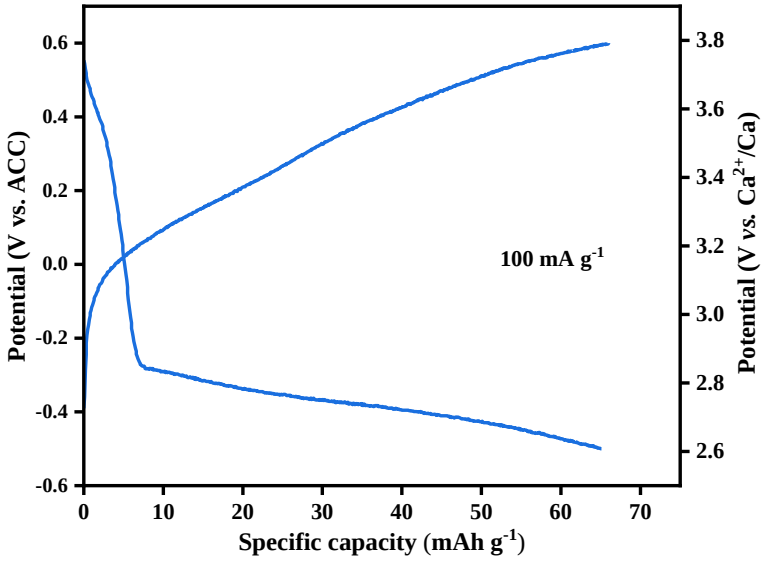

Figure S13. The galvanostatic charge/discharge profiles of PANI at 100 mA g^{-1}.

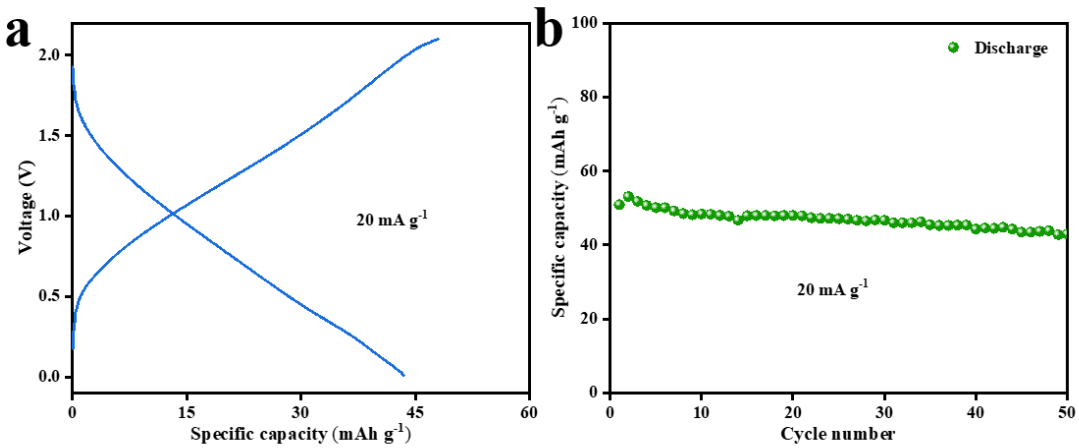

Figure S14. The electrochemical performance of PANI//Ca_xVO_2(B)/rGO at 50 ℃. a) Galvanostatic charge/discharge profiles at 20 mA g^{-1}; b) Cycling performance at 20 mA g^{-1}.

Table S2. The Ca^{2+} storage performance of VO_2(B)/rGO and the reported inorganic cathode materials for CIBs with organic electrolyte.

Cathode	Counter/reference electrode	Electrolyte	Working temperature	Specific capacity (mAh g^{-1}) /current density (mA g^{-1})	Current density (mA g^{-1})/capacity retention (%) /Specific capacity (mAh g^{-1}) / Cycle number	Reference
VO_2(B)/rGO	ACC/–	0.3 M $Ca(TFSI)_2$ in G4	Room temperature (RT)	319.2/20 262.2/50 210.2/100 168/200 112.4/500 72.4/1000 307.3/50 268.4/100 231.4/200 158/500 113.9/1000 89.7/1500 73.3/2000	500/85/136.2/3000	This work
			50 ℃		1000/85/108.2/3000	This work
$Mg_xV_2O_5{\cdot}nH_2O$	ACC/–	0.8 M $Ca(TFSI)_2$ in EC: PC: EMC: DMC	RT	195.5/20 137/50 126.2/100	100/98.6/126.2/150	[6]
			50 ℃	142.4/100	1000/93.6/59.2/2500	
$NaV_2(PO_4)_2F_3$	ACC/–	0.25 M $Ca(PF_6)_2$ in EC: PC: EMC: DMC	RT	110/10 95/100 85/200 65/500	200/81/55/2000	[7]
$Na_{0.5}VPO_{4.8}F_{0.7}$	ACC/–	1.0 M $Ca(PF_6)_2$ in EC/PC	RT	88/25 75/50 62/100	50/90/67.5/500	[8]
δ-MnO_2	ACC	0.5 M $Ca(TFSI)_2$	RT	125/100 118/200 105/500	100/54/67/50	[9]
$CaV_6O_{16}{\cdot}2.8H_2O$	ACC/–	0.3 M $Ca(TFSI)_2$/G_2	RT	131.7/50 44.9/500	500/94.4/42.4/1000	[10]
			50 ℃	170.8/50 134.7/100	500/93/70/1000	

				104.0/200 65.0/500 47.7/800 41.2/1000		
β-$Ca_{0.14}V_2O_5$	ACC	1.0 M $Ca(BF_4)_2$ in EC: PC	RT	247/20 150/50 74.8/100	100/82/60.9/400	[11]
$NaV_2(PO_4)_3$	ACC/–	1 M $Ca(TFSI)_2$ in ACN	RT	81/3.5	–	[12]
Se/CMK-3	ACC	0.25 M $Ca(TFSI)_2$ in EC/DMC	RT	~476/50 300/100 250/200 200/500	500/100/150/300	[13]
$VOPO_4{\cdot}2H_2O$	ACC/–	0.8 M $Ca(TFSI)_2$ in EC: PC: EMC: DMC	RT	86/20 42.7/200	100/~65/50/200	[14]
VS_4/rGO	Ca/–	$Ca[B(hfip)_4]_2$ in DME	RT	315/100	–	[15]
Na-doped $NH_4V_4O_{10}$	Pt/Ag-Ag^+	$Ca(ClO_4)_2{\cdot}xH_2O$ in ACN	RT	150/100 92/300 72/500	100/100/150/100	[16]
$Fe_4[Fe(CN)_6]_3$	Graphite rod/Ag-Ag^+	1 M $Ca(ClO_4)_2$ in ACN	RT	120/125	125/85.8/103/80	[17]
$FeV_3O_9{\cdot}1.2H_2O$	ACC/–	0.5 M $Ca(ClO_4)_2$/AN	RT	303/20 200/50 105/200	200/79/83/400	[18]
$Ca_{0.13}MoO_3{\cdot}(H_2O)_{0.41}$	ACC/–	0.5 M $Ca(ClO_4)_2$/AN	RT	192/85.65 138/171.3 109/342.6	342.6/94/85.3/50	[19]
CuS	Ca/–	0.8 M $Ca(TFSI)_2$ in EC: PC: EMC: DMC	RT	200/100	100/50/100/30	[20]
MnO_2/PANI	ACC/–	0.5 M $Ca(TFSI)_2$/AN	RT	150/100 140/200 134/500 120/1000	1000/~50/62/5000	[21]
$Ti_2O(PO_4)_2(H_2O)$	ACC/–	0.5 M $Ca(BF_4)_2$ in EC:PC RT	RT	101.1/20 60.8/50 38.5/100 17.2/200	50/95/57.8/1500	[22]

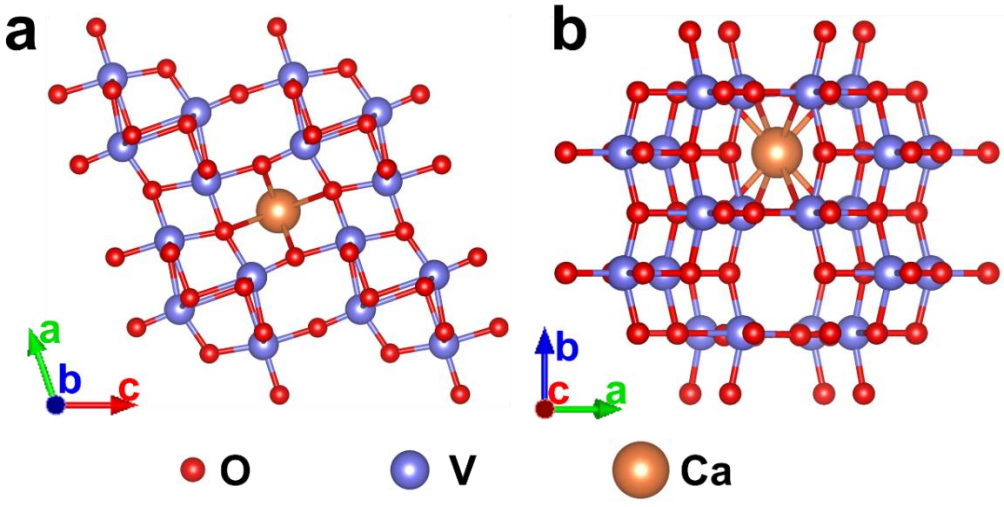

Figure S15. The configurations of Ca-inserted VO_2(B) along the a) *b*-axis and b) *c*-axis.

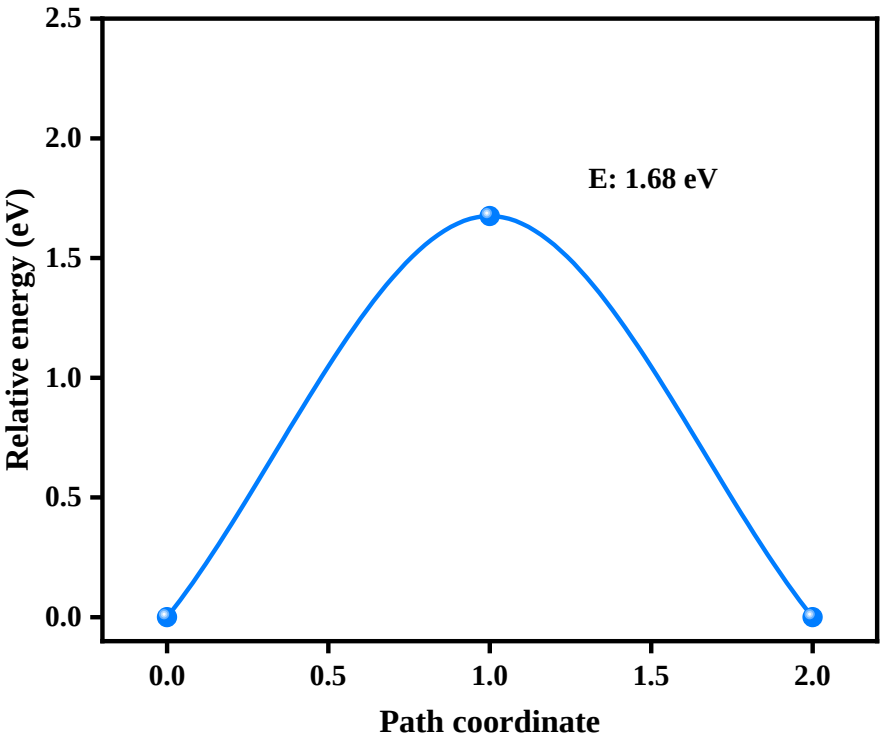

Figure S16. The diffusion energy barrier profile of Ca^{2+} migration along the *b* direction in VO_2(B).

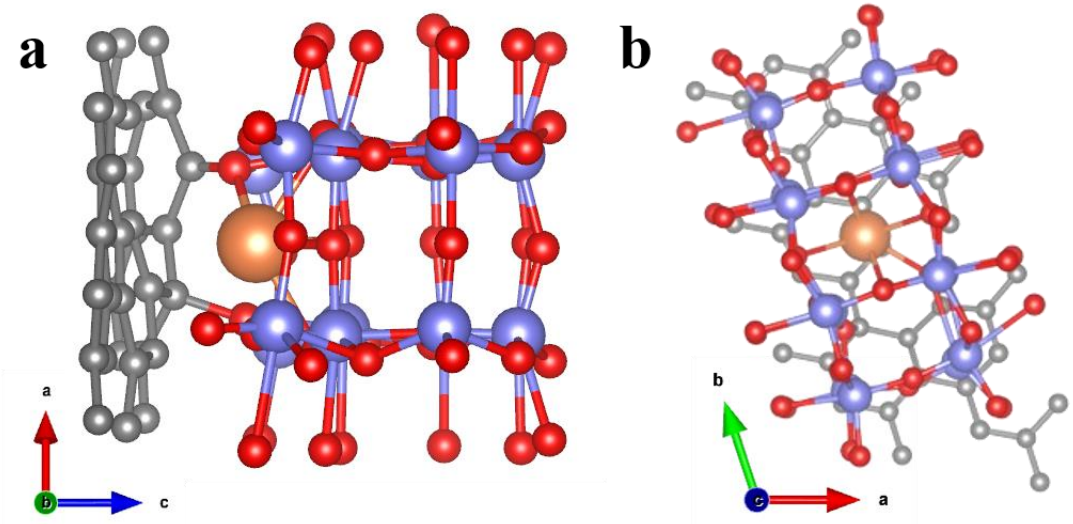

Figure S17. The configurations of Ca-inserted VO_2(B)/rGO along the a) *b*-axis and b) *c*-axis.

Table S3. The comparison of diffusion energy barrier of Ca^{2+} in commonly used cathode materials for CIBs.

Cathode Materials	Diffusion Energy Barriers	References
VO_2(B)/rGO	Intra-Unit：1.675 eV Interface：0.64 eV	This work
$NaV_2(PO_4)_2F_3$	Intra-Unit：0.268 eV Inter-Unit Paths：0.785 eV	[7]
$Ca_xNa_{0.5}VPO_{4.8}F_{0.7}$	Intra-Unit：0.243 eV Inter-Unit Paths：0.606 eV	[8]
$CaV_6O_{16} \cdot 2.8H_2O$	0.36 eV	[10]
MnO_2@PANI	0.221 eV	[21]

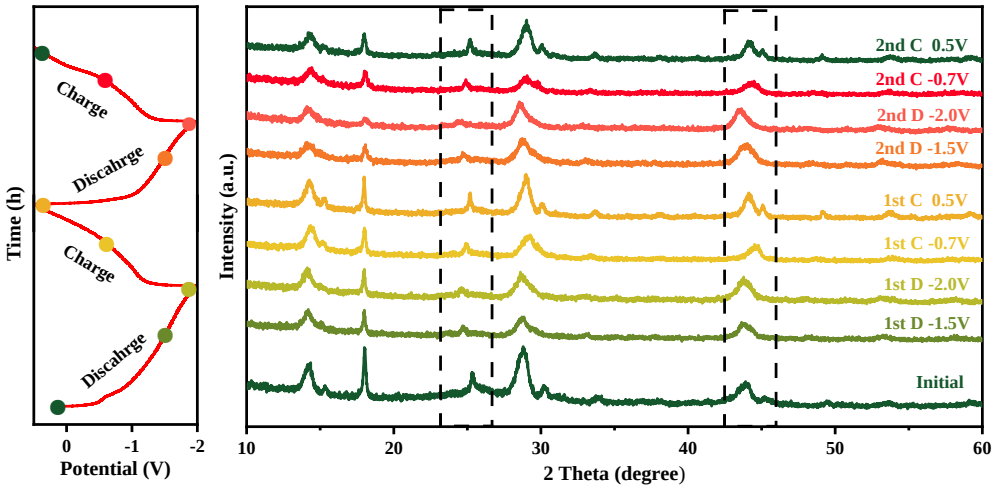

Figure S18. *Ex-situ* XRD patterns of VO_2(B)/rGO at different states.

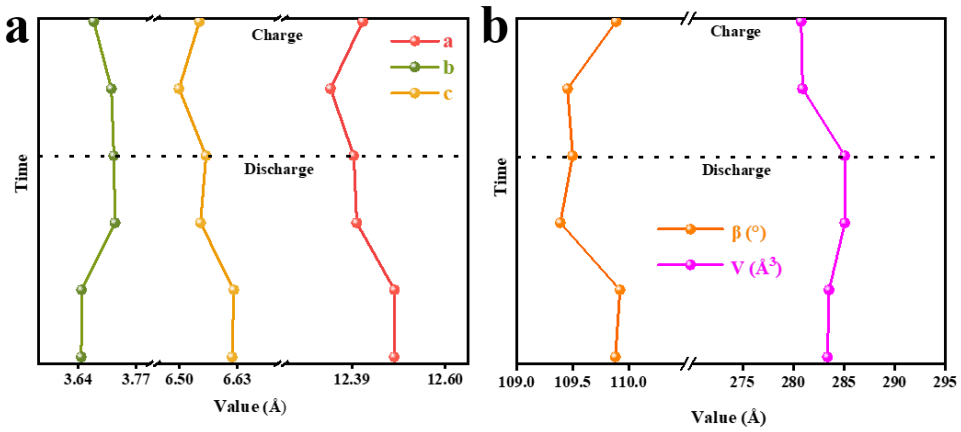

Figure S19. Corresponding lattice constant evolution of VO_2(B)/rGO in the first cycle.

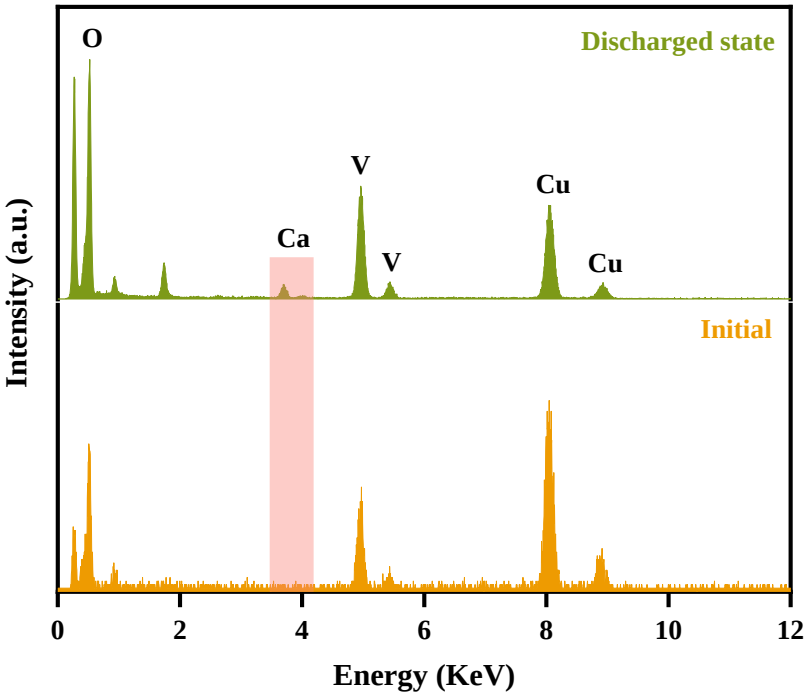

Figure S20. EDX spectra of VO_2(B)/rGO at initial and discharged states.

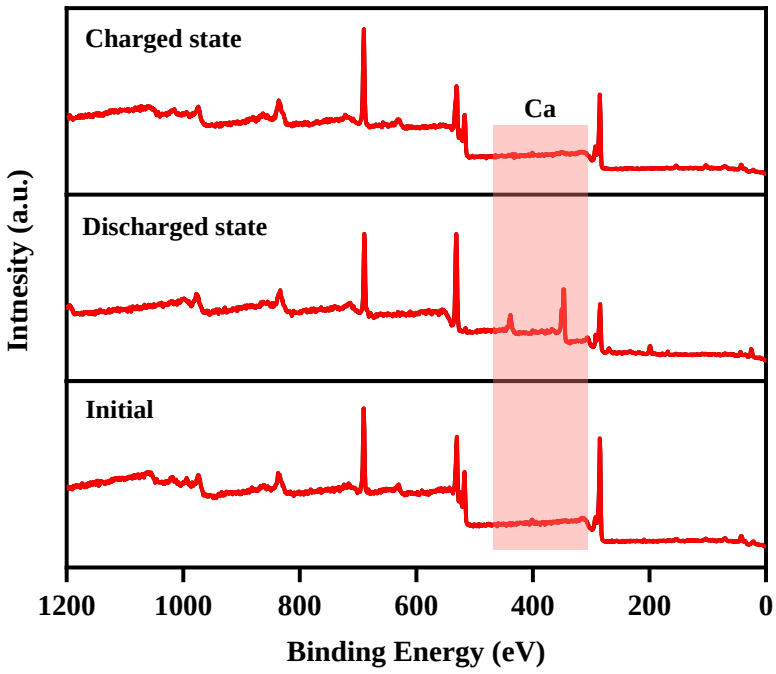

Figure S21. The wide XPS spectrum of VO_2(B)/rGO at different states.

Table S4. The quantitative elemental ratios of VO_2(B)/rGO at different states.

	Ca
Initial state	0.23%
Discharge state	8.99%
Charge state	0.83%

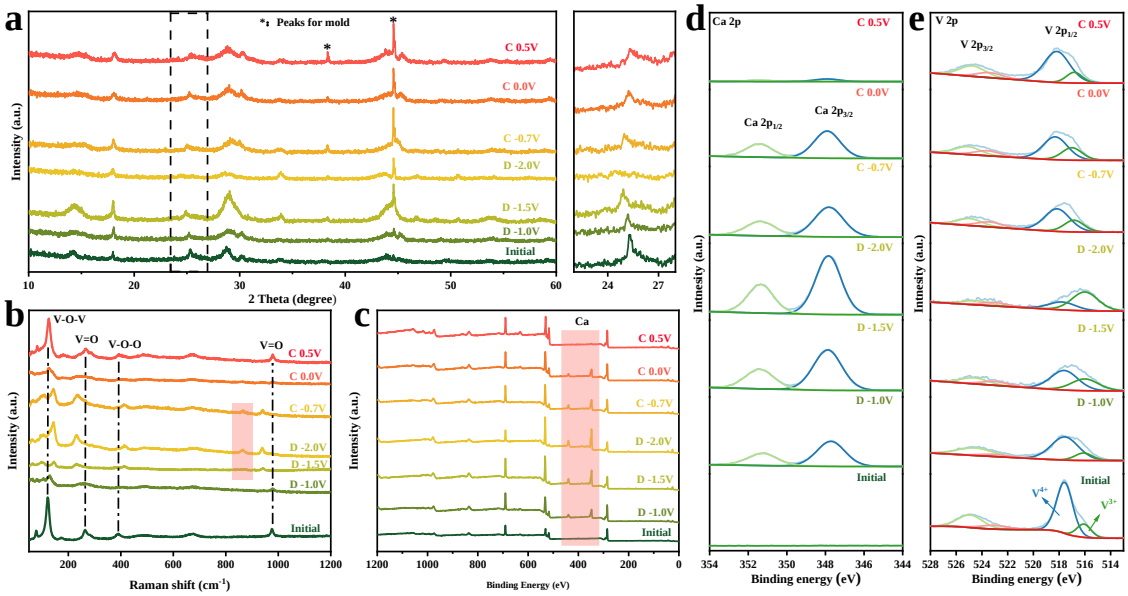

Figure S22. Calcium storage mechanism of VO_2(B)/rGO at 50 ℃. a) *Ex-situ* XRD patterns and b) *Ex-situ* Raman patterns of VO_2(B)/rGO; c) The wide XPS spectrum of VO_2(B)/rGO at different states; *Ex-situ* XPS spectra of d) Ca 2p and e) V 2p for VO_2(B)/rGO at different states.

Upon discharging to –2 V, the XRD peaks at 25.3°, corresponding to the (110) crystal plane shift to lower angles, suggesting that Ca^{2+} is gradually intercalated into the tunnel structures of VO_2(B) and thus expands the unit cell (Figure S22a). In contrast, when charged to 0.5 V, these peaks shift reversibly to the initial locations, demonstrating the good structural reversibility. Figure S22b shows the *ex-situ* Raman spectra. During the discharge process, two Raman peaks at 270 and 1013 cm^{-1} shift to lower wavenumbers, and shift reversely back to the original positions during the Ca^{2+} extraction process. The low-wavenumber peaks at 163 cm^{-1} and 400 cm^{-1} show the opposite periodic shift to the above two peaks. A new peak at 876 cm^{-1} appears, which is probably derived from the formation of stretching vibration of O-Ca in VO_2(B)/rGO during the charge-discharge process. In contrast to the initial situation, the peak of Ca 2p emerges and has high intensity at fully discharged states, further demonstrating that Ca^{2+} are inserted into VO_2(B)/rGO (Figure S22c-d). At the charged state, the content of Ca reduces and a small fraction of residual Ca^{2+} exists in the VO_2(B)/rGO. Most of the V^{4+} is reduced to V^{3+}

after discharge (Figure S22e), and V^{3+} is oxidized back to V^{4+} at the subsequent charging process.

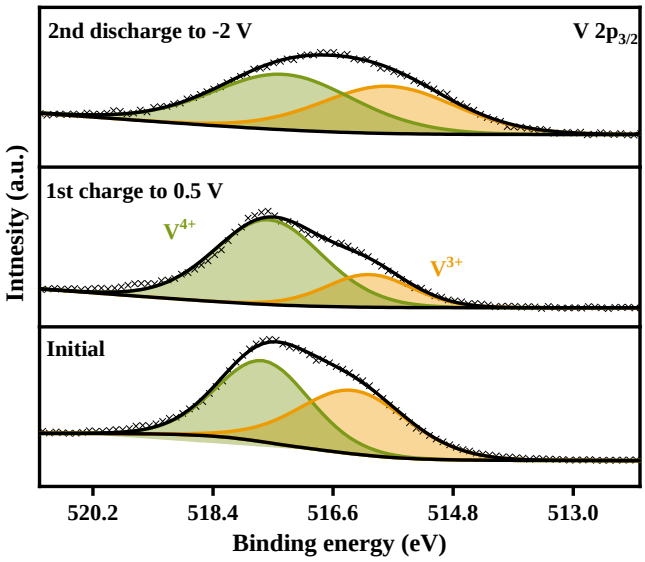

Figure S23. *Ex-situ* XPS spectra of V 2p for VO_2(B) at different states.

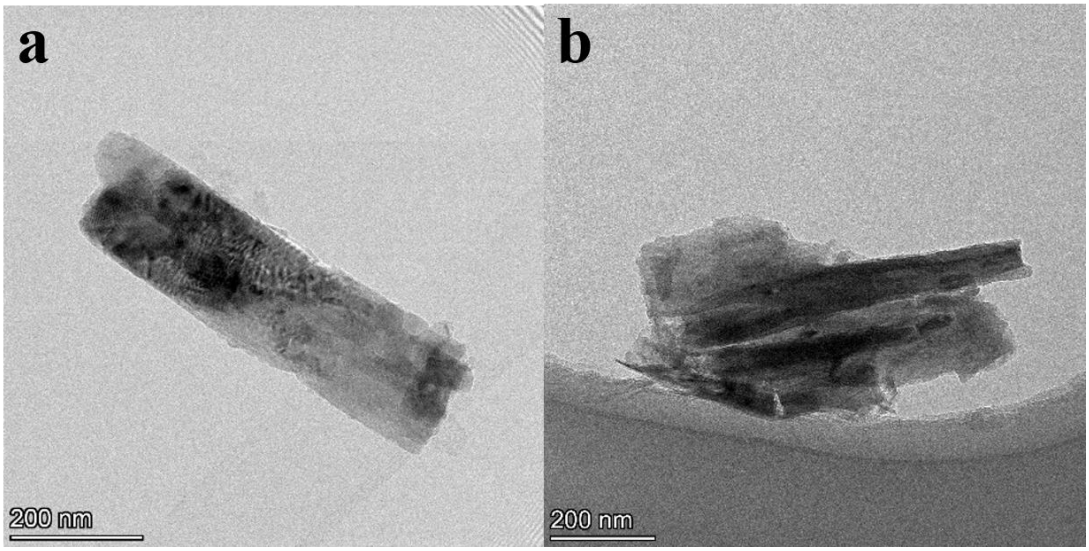

Figure S24. The TEM images of a) fully discharged VO_2(B)/rGO and b) fully charged VO_2(B)/rGO.

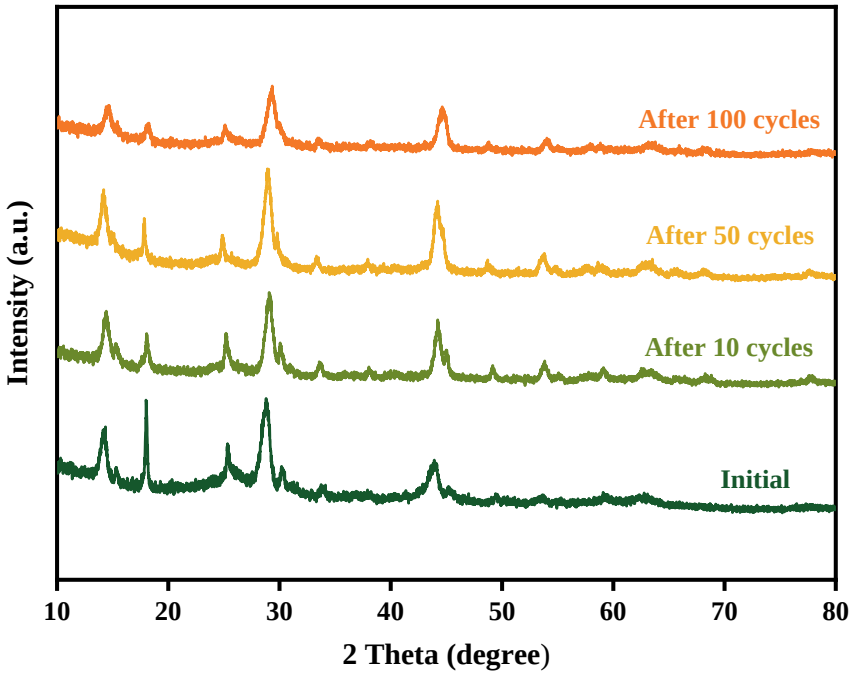

Figure S25. The XRD patterns of VO_2(B)/rGO electrodes after 10, 50, and 100 cycles.

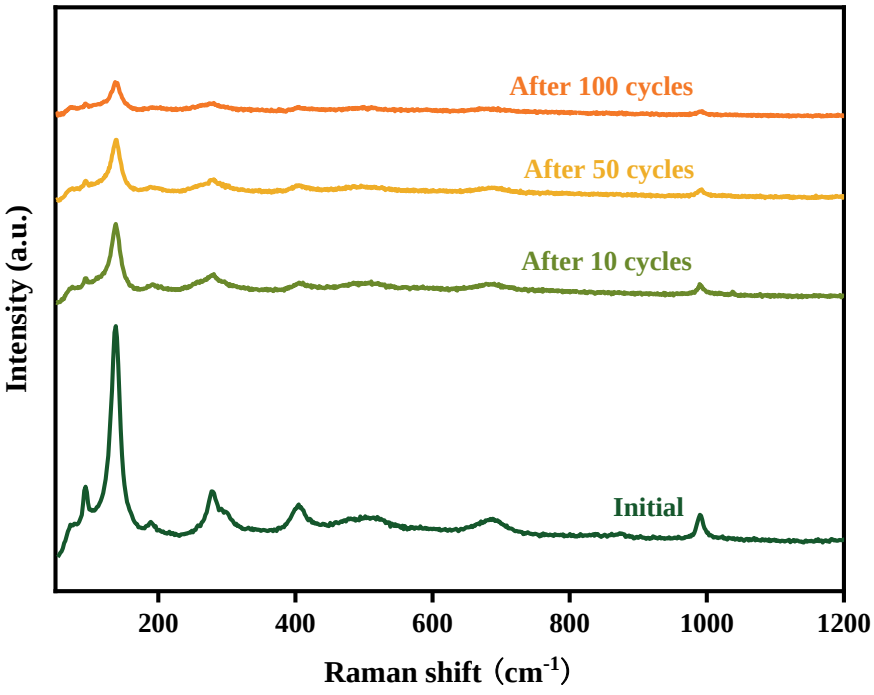

Figure S26. The Raman spectrums of VO_2(B)/rGO electrodes after 10, 50 and 100 cycles.

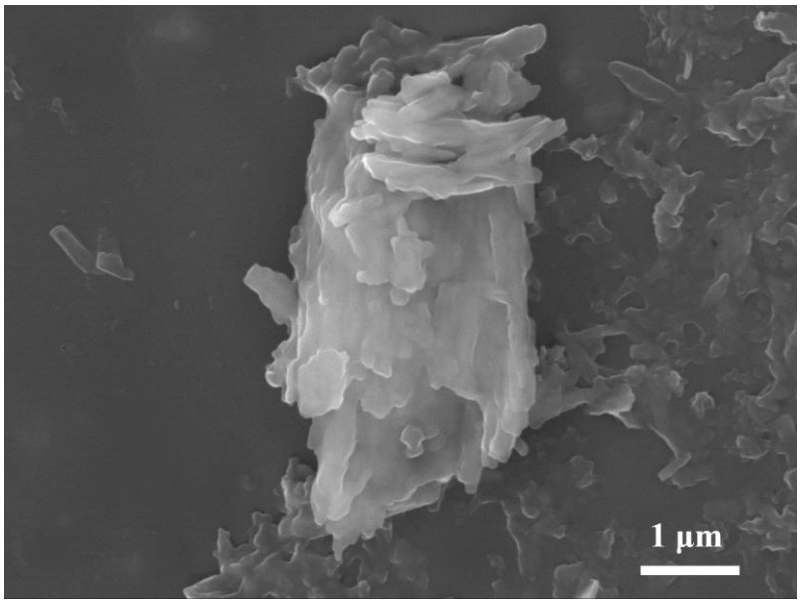

Figure S27. The SEM image of VO_2(B)/rGO after 100 cycles.

Reference

[1] Kresse, Furthmuller, *Phys. Rev. B* **1996**, 54, 11169.

[2] J. P. Perdew, K. Burke, M. Ernzerhof, *Phys. Rev. Lett.* **1996**, 77, 3865.

[3] G. Kresse, D. Joubert, *Phys. Rev. B* **1999**, 59, 1758.

[4] S. Grimme, J. Antony, S. Ehrlich, H. Krieg, *J. Chem. Phys.* **2010**, 132, 19.

[5] G. Henkelman, B. P. Uberuaga, H. Jonsson, *J. Chem. Phys.* **2000**, 113, 9901.

[6] X. Zhang, X. M. Xu, B. Song, M. Y. Duan, J. S. Meng, X. P. Wang, Z. T. Xiao, L. Xu, L. Q. Mai, *Small* **2022**, 18, 7.

[7] C. H. Chen, F. Y. Shi, S. S. Zhang, Y. Q. Su, Z. L. Xu, *Small* **2022**, 18, 9.

[8] Z. L. Xu, J. Park, J. Wang, H. Moon, G. Yoon, J. Lim, Y. J. Ko, S. P. Cho, S. Y. Lee, K. Kang, *Nat. Commun.* **2021**, 12, 9.

[9] C. L. Zuo, F. Y. Xiong, J. J. Wang, Y. K. An, L. Zhang, Q. Y. An, *Adv. Funct. Mater.* **2022**, 32, 8.

[10] J. J. Wang, J. X. Wang, Y. L. Jiang, F. Y. Xiong, S. S. Tan, F. Qiao, J. H. Chen, Q. Y. An, L. Q. Mai, *Adv. Funct. Mater.* **2022**, 32, 8.

[11] S. J. Richard Prabakar, A. B. Ikhe, W. B. Park, D. Ahn, K. S. Sohn, M. Pyo, *Adv. Funct. Mater.* **2023**.

[12] S. Kim, L. Yin, M. H. Lee, P. Parajuli, L. Blanc, T. T. Fister, H. Park, B. J. Kwon, B. J. Ingram, P. Zapol, R. F. Klie, K. Kang, L. F. Nazar, S. H. Lapidus, J. T. Vaughey, *ACS Energy Lett.* **2020**, 5, 3203.

[13] R. Zhou, Z. Hou, Q. Liu, X. Q. Du, J. Q. Huang, B. A. Zhang, *Adv. Funct. Mater.* **2022**, 32, 9.

[14] J. J. Wang, S. S. Tan, F. Y. Xiong, R. H. Yu, P. J. Wu, L. M. Cui, Q. Y. An, *Chem. Commun.* **2020**, 56, 3805.

[15] Z. Y. Li, B. P. Vinayan, P. Jankowski, C. Njel, A. Roy, T. Vegge, J. Maibach, J. M. G. Lastra, M. Fichtner, Z. Zhao-Karger, *Angew. Chem.-Int. Edit.* **2020**, 59, 11483.

[16] T. N. Vo, H. Kim, J. Hur, W. Choi, I. T. Kim, *J. Mater. Chem. A* **2018**, 6, 22645.

[17] N. Kuperman, P. Padigi, G. Goncher, D. Evans, J. Thiebes, R. Solanki, *J. Power Sources* **2017**, 342, 414.

[18] M. S. Chae, D. Setiawan, H. J. Kim, S. T. Hong, *Batteries-Basel* **2021**, 7, 9.

[19] M. S. Chae, H. H. Kwak, S. T. Hong, *ACS Appl. Energ. Mater.* **2020**, 3, 5107.

[20] W. Ren, F. Y. Xiong, Y. Q. Fan, Y. L. Xiong, Z. L. Jian, *ACS Appl. Mater. Interfaces* **2020**, 12, 10471.

[21] C. L. Zuo, F. Y. Chao, M. Li, Y. H. Dai, J. J. Wang, F. Y. Xiong, Y. L. Jiang, Q. Y. An, *Adv. Energy Mater.* **2023**, 10.

[22] S. J. R. Prabakar, W. B. Park, J. Y. Seo, S. P. Singh, D. Ahn, K. S. Sohn, M. Pyo, *Energy Storage Mater.* **2021**, 43, 85.